Absolute Magnetometry with ^{3}He

Midhat Farooq,[1] Timothy Chupp,[1,*] Joe Grange,[1,2] Alec Tewsley-Booth,[1] David Flay,[3] David Kawall,[3] Natasha Sachdeva,[1] and Peter Winter[2]

[1]*Physics Department, University of Michigan, Ann Arbor, Michigan 48109, USA*
[2]*Argonne National Laboratory, Lemont, Illinois 60439, USA*
[3]*Physics Department, University of Massachussetts, Amherst, Massachussetts 01003, USA*

(Received 17 January 2020; accepted 1 May 2020; published 5 June 2020)

We report development of a highly accurate (parts per billion) absolute magnetometer based on ^{3}He NMR. Optical pumping polarizes the spins, long coherence times provide high sensitivity, and the ^{3}He electron shell effectively isolates the nuclear spin providing accuracy limited only by corrections including materials, sample shape, and magnetization. Our magnetometer was used to confirm calibration, to 32 ppb, of the magnetic-field sensors used in recent measurements of the muon magnetic moment anomaly $(g_\mu - 2)$, which differs from the standard model by 2.4 ppm. With independent determination of the magnetic moment of ^{3}He, this work will lead the way to a new absolute magnetometry standard.

DOI: 10.1103/PhysRevLett.124.223001

Magnetometry, determining the intensity of a magnetic field over space and time, is crucial to many fields of applied and fundamental science including medicine, materials science, geology and geodesy, astronomy, and fundamental physics. Often-competing magnetometry requirements include sensitivity, stability, absolute accuracy, bandwidth, and spatial resolution, and many applications require accurately determining the magnetic field intensity in Tesla $(\mathrm{kg}\cdot\mathrm{s}^{-2}\cdot\mathrm{A}^{-1})$. The most sensitive magnetometers, superconducting quantum-interference devices (SQUIDs) reach sub $\mathrm{fT}/\sqrt{\mathrm{Hz}}$ sensitivity [1], but are not absolute. Optically pumped atomic magnetometers approach this sensitivity in small fields [2,3], but are generally not highly accurate or stable. Accurate absolute magnetometers include rotating coils [4] and calibrated NMR [5].

Magnetic fields are most accurately determined by measuring the *frequency* corresponding to the energy difference of two quantum states. The frequency ω and magnetic field B are related by $B = \omega(\hbar J/|\mu|) = \omega/|\gamma|$, where $\hbar J$ is the total angular momentum, μ is the magnetic moment, and $\gamma = \mu/\hbar J$. $J = 1/2$ nuclei in diamagnetic materials are the most nearly ideal two-state quantum systems, and NMR of proton rich substances, e.g., H_2O, is most commonly encountered. For pure H_2O, the shielded proton magnetic moment for a spherical sample at 25° $\mu'_p(25°)$ is known to 11.3 ppb, limited mostly by measurement of $\mu'_p/\mu_e(H)$ [6,7].

In practical magnetometry, temperature-dependent sample, shape, and external material effects lead to perturbations of the magnetic field that must be calibrated or corrected. With much smaller intrinsic corrections illustrated by the practically engineered magnetometer demonstrated in this Letter, a new more precise and more accurate standard for magnetometry can be established with ^{3}He. Unlike H_2O, for which the signal size is proportional to $1/T$, the ^{3}He is hyperpolarized by laser optical pumping techniques; thus ^{3}He magnetometry is applicable over a very broad range of magnetic fields using NMR for fields >0.1 T and atomic sensors for lower fields [8].

Quantities relevant to determining the magnetic moment of a free ^{3}He atom are provided in the Supplemental Material [9]. Diamagnetic shielding of the atomic electrons reduces the field at the ^{3}He nucleus, referred to as the helion. The shielded helion moment μ'_h has been measured to 4.3 ppb relative to the shielded proton magnetic moment in water [33] and to 4 ppb relative to protons in high-pressure H_2 [34], but the uncertainty on μ'_h, 11.4 ppb, is dominated by the uncertainty on $\mu'_p/\mu_e(H)$. To eliminate the proton from the chain, effort is underway [35,36] to directly measure the magnetic moment of the unshielded nucleus μ_h in a Penning trap using techniques similar to those used to measure the proton [37] and antiproton [38] g factors. The high-precision theoretical calculation of the diamagnetic shielding [39], which is only weakly temperature dependent, would provide the shielded magnetic moment μ'_h at the few ppb level.

The muon magnetic moment anomaly—A spin $\frac{1}{2}$-particle (lepton) with charge q_l and mass m_l has a magnetic moment $\mu_l = g_l(q_l/2m_l)\hbar/2$. For a structureless particle with no radiative corrections $g_l = 2$ [40], however, interactions with the virtual fields of the quantum vacuum lead to corrections, and $g_l = 2(1 + a_l)$ [41–43]. The largest correction, ≈0.1%, is due to QED with the strong and weak interactions entering at 3 and 6 orders of magnitude less, respectively. For the muon, the most recent standard model determinations a_μ^{SM} are summarized in [44,45]. The muon magnetic-moment

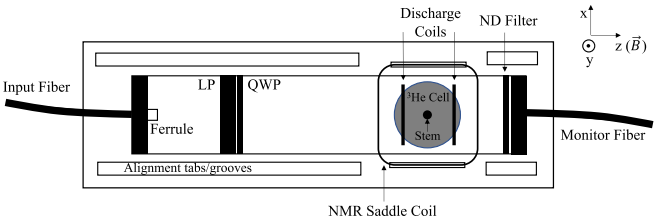

FIG. 1. The ^{3}He magnetometer assembly described in the text. The assembly is 5 cm square in cross section and 15 cm long. The distance from the input-fiber ferrule to the cell is approximately 8 cm. LP and QWP indicate the linear polarizer and quarter wave plate.

anomaly has been measured by producing muons in accelerators at CERN [46] and Brookhaven [47]. The most recent measurements $a_\mu^{\rm exp}$ from Brookhaven (E821) for μ^+ [48] and μ^- [49] reveal $a_\mu^{\rm exp} - a_\mu^{\rm SM} = (28.0 \pm 7.4) \times 10^{-10}$ or $(2.40) \pm (0.63)$ ppm, using $a_\mu^{\rm SM}$ from [45]. A new measurement with higher statistical precision and smaller systematic errors is underway at Fermilab and is expected to improve the uncertainty by a factor of 4 [50].

Experimentally, muons are confined in a 7.1 m radius magnetic storage ring with weak vertical focusing by electric quadrupole fields. The anomaly frequency, determined from the variation of the rate of μ decays into positrons or electrons that exceed a threshold energy, is $\omega_{a_\mu} \approx a_\mu (e/m_\mu)\tilde{B}$ for muon momentum near 3.094 GeV/c, where the electric field effects are effectively canceled. The field averaged over the detected muon trajectories and time is $\tilde{B} \approx 1.45$ T. A chain of measurements using proton-NMR magnetometers (probes) calibrated with high-purity H_2O yields the frequency $\tilde{\omega}'_p = (2|\mu'_p|/\hbar)\tilde{B}$. In terms of ω_{a_μ} and $\tilde{\omega}'_p$,

$$a_\mu = \frac{g_e}{2}\frac{\omega_{a_\mu}}{\tilde{\omega}'_p}\left|\frac{\mu'_p}{\mu_e}\right|\frac{m_\mu}{m_e}, \tag{1}$$

where μ'_p/μ_e is determined to 10.5 ppb [9], g_e has been determined to 0.28 ppt [51], and m_μ/m_e is determined to 22 ppb from the muonium hyperfine splitting [52] and QED [7]. In this work, the ^{3}He magnetometer independently determined and confirmed the systematic corrections to the standard H_2O reference probes used in E821.

The ^{3}He Magnetometer—The magnetometer illustrated in Fig. 1 is a compact device designed to operate at 1.45 T providing polarization and NMR magnetometry *in situ*. The required elements are the ^{3}He sample contained in a glass cell, coils to excite a discharge in the ^{3}He, the NMR coil for excitation and pickup of free-precession, optical fibers to guide the incident optical pumping light and to monitor transmission through the cell for laser tuning, circular polarization optics, and the mounting structure. The design principles require removing all ferromagnetic materials including electronic components and cables, minimizing materials near the ^{3}He sample and fabricating as closely as possible cylindrically or spherically symmetric distributions of materials.

The magnetometer was assembled in a 3D printed mount with grooves that aligned the components. In our initial (Mark-I) assemblies the mount was polylactic acid thermoplastic (PLA) with a square cross section "clamshell" for ease of mounting, alignment, and access for cell orientation and material perturbation studies. The plastic mount was enclosed in 0.002-inch thick copper folded from a flat sheet and soldered at the joints. The ^{3}He cells were blown borosilicate (PYREX) glass, approximately spherical with 2.5 cm diameter and a stem several mm long (see Supplemental Material [9]). Several ^{3}He pressures were investigated, and 10 torr (20 °C) provided the best combination of polarization lifetime, free-precession relaxation time (T_2^*), and signal size.

Optical pumping of metastable ^{3}He or MEOP has been extensively studied, most recently at high magnetic fields relevant to this work [9,53–55]. A discharge was excited by radio frequency (4–6 MHz) applied to a 2-cm-diameter coil pair in contact with the outside of the glass cell. The input fiber provided optical pumping light from a 1083 nm, 2W fiber-amplified laser [56]. For development studies at 2–3 mT an optical polarimeter monitored the circular polarization of the 668 nm fluorescence indicating 30–50% ^{3}He polarization [57]. We did not directly measure the ^{3}He polarization at 1.45 T, however, NMR signal sizes and system parameters were consistent with 4%–8% in the 10-torr cell. The polarization (discharge on) time was typically 1–2 minutes, and the polarization lifetime was greater than five hours.

The ^{3}He NMR system consisted of a saddle coil surrounding the ^{3}He cell that produced a field along the y axis. The NMR coil, matched to 50 Ω and tuned to the ^{3}He resonant frequency $\omega'_h/(2\pi) \approx 47.1$ MHz, provided both the NMR pulse and inductive pickup. The coil was connected to the NMR controller described in the Supplemental Material [9]. The mixer reference frequency was set below the precession frequency, and the 100–300 Hz mixed-down signal was digitized. An identical NMR controller for the H_2O probes was tuned to 61.7 MHz and interfaced to the same data acquisition system. The NMR tip angle was ≈23° for ^{3}He leaving about 90% of the longitudinal polarization after each pulse and providing variation of the longitudinal and transverse magnetization for systematic studies. The 90° pulse for H_2O protons maximized the signal size. The pulse and mixer reference frequencies for both the ^{3}He and proton (H_2O) channels and the data acquisition sample trigger were generated by separate function generators all locked to a single rubidium clock. Details of the NMR signal processing and data blinding are discussed in the Supplemental Material [9].

Calibration of ^{3}He and E821 H_2O probes—The two H_2O probes used in E821, one with a spherical sample and

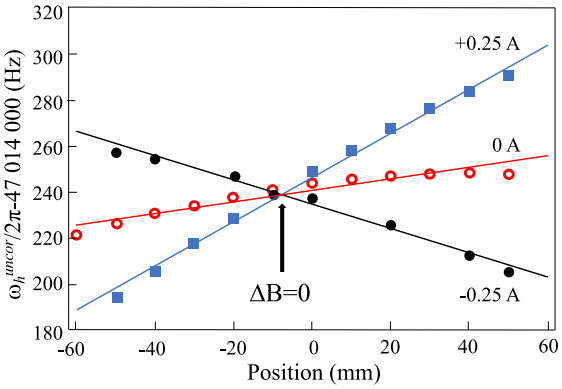

FIG. 2. Scan of the ^{3}He frequency as the magnetometer was translated along z with positive and negative gradient currents showing the $\Delta B = 0$ position z_0. The solenoid's higher order (quadratic) gradients are evident; straight lines are provided to guide the eye.

one with a cylindrical sample, are described in detail in Ref. [58]. The calibration of each H_2O probe to ^{3}He used a precision-shimmed superconducting solenoid magnet. The magnetic field drift was dominated by a diurnal cycle and was less than 60 ppb over the five hour calibration measurements. The ^{3}He magnetometer and H_2O probes were mounted on a translation stage, and a positive or negative linear gradient along each axis was applied by rapidly ($\lesssim$1 min) reversing the gradient-coil currents to determine a unique position (x_0, y_0, z_0), the $\Delta B = 0$ position. Adjusting each probe to find x_0 and y_0 then required only translation along the z axis to position each probe at the $\Delta B = 0$ position indicated in Fig. 2.

Calibration studies of the two H_2O probes were undertaken on separate days, with small modifications to the ^{3}He setup between the two studies. Figure 3 shows the

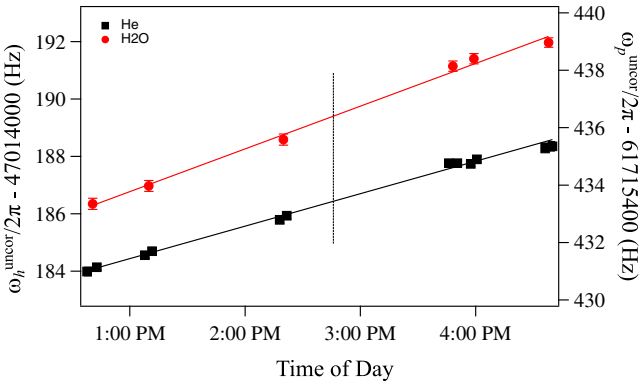

FIG. 3. Uncorrected frequencies for ^{3}He (left axis) and the cylindrical H_2O probe (right axis); the solid lines are linear fits vs time. The χ^2_ν, 1.0 and 1.2, respectively, for ^{3}He and H_2O, are accounted for in the magnetic drift uncertainties. The vertical dotted line indicates the time to which all frequencies are interpolated. Both scales span 10 Hz. The different slopes are due to the different magnetic moments.

uncorrected frequencies $\omega_3^{\mathrm{uncor}}$ and $\omega_p^{\mathrm{uncor}}$ as a function of time during calibration of the cylindrical H_2O probe showing the effect of the magnetic-field drift. All frequency measurements were interpolated to the average time of the ^{3}He measurements indicated by the vertical dotted line in Fig. 3. Corrections were applied to both species' interpolated frequencies to provide the two shielded frequencies ω_3' and ω_p' for each H_2O probe at the specified position and time.

Corrections and uncertainties—Corrections, determined independently within one day of each calibration study, are presented in Table I. Corrections fall into four categories: materials external to the sample, sample container materials, sample-material magnetization effects, and temperature dependence. Though all of these are in principle applicable to both species, the size and method of determining the corrections differed significantly.

External materials include all components of a probe, cables, translation stage and mounting structure other than the sample and glass sample container. All effects of external materials were measured with an auxiliary vaso-line-sample NMR probe at the $\Delta B =$ position with and without the ^{3}He assembly or H_2O probe. The auxiliary probe temperature was not monitored ($|\frac{d\omega_{aux}}{dT}| \approx 2.5$ ppb/°C [59]), and uncertainties including those due to temperature variations were estimated from the scatter of multiple measurements. Because the NMR coil inhibited positioning of the auxiliary probe at the exact position of the ^{3}He cell, and because the $\Delta B = 0$ positioning could not be checked with the ^{3}He cell removed, the auxiliary probe was moved back and forth a few millimeters over the cell position to estimate the uncertainty due to position misalignment.

For the H_2O probe, ± 10 ppb variations when rotating the probe around the probe axis were reported by [58] and confirmed for this work. Rotations of the stem with respect to the axis of the magnet with polar angle $\theta = 0$ and 90° and with $\phi = 0$ and 90° were consistent with modeling the stem as a magnetic dipole, which predicted $P_2(\cos\theta)$ dependence at the cell center. For the H_2O calibration measurements, the stem was oriented along y ($\theta = 90°$); extrapolating to the magic angle $\theta = 54°$ resulted in the correction of -0.61 ± 0.20 Hz. The stem also caused magnetic gradients, which resulted in a factor of 2 shorter T_2^* with $\theta = 0°$. Rotation of the cell around the stem axis showed variations of 0.35 Hz, included as an uncertainty. The same ^{3}He cell and stem orientation corrections were applied for both H_2O probes. In principle, there was also a correction for the different displacement of air (≈20% paramagnetic O_2) by the sample and the auxiliary probe. For a spherical ^{3}He sample, this effect would vanish. Modeling the air displaced by the stem as a dipole, the magnetic field at the center of the cell has an amplitude less than about 20 fT and correction $<1\,\mu$Hz. For the H_2O probes, the sample was not removed, and there was no correction.

TABLE I. Corrections and uncertainties for cross-calibration studies of both H_2O probes. For entries with correction < 0.01 Hz, the correction is indicated with a 0; entries that do not apply for a specific probe are indicated with $\cdots$; the * indicates that one correction or uncertainty applies to both studies. The last two lines provide new determinations from this work to be compared to $|R'_{hp}| = 0.7617861313(33)$ and $|\mu'_{hp}| = 1.074553090(13)$ based on Ref. [33]. To convert frequency uncertainties to approximate ppb, divide by 47.1×10^{-3} for ^{3}He and 61.7×10^{-3} for H_2O.

	Spherical H_2O (Hz)				Cylindrical H_2O (Hz)			
	H_2O		^{3}He		H_2O		^{3}He	
Source	Corr.	Unc.	Corr.	Unc.	Corr.	Unc.	Corr.	Unc.
External materials	10.61	0.49	21.38	1.22	13.82	0.49	23.64	1.13
Probe materials	2.71	0.62	…	…	2.90	0.62	…	…
H_2O Probe-material asymmetry*	0	1.24	…	…	0	1.24	…	…
^{3}He glass stem*	…	…	−0.61	0.20	…	…	−0.61	0.20
^{3}He cell rotation*	…	…	0	0.35			0	0.35
Sample magnetization	0	0	0	0.20	−93.10	0.26	0	0.18
Radiation damping*	…	…	0	0.18	…	…	0	0.18
$\sigma_p^{H_2O}$ Temperature dependence	−0.48	0.64	…	…	−1.27	0.64	…	…
χ^{H_2O} Temperature dependence	0	0	…	…	0	0.02	…	…
Total of corrections	12.84	1.60	20.77	1.31	−77.65	1.62	23.05	1.23
Frequency extraction unc.	0.01		…		0.10		…	
Magnet drift uncertainty	0.05		0.09		0.18		0.12	
Position uncertainty*	0.07		0.05		0.07		0.05	
Total unc.	1.61		1.32		1.64		1.23	
$\omega'/2\pi$	61 710 229.90		47 009 998.24		61 715 758.45		47 014 209.45	
$B - 1\,449\,000\,000$ (nT)	400 419 (41)		400 448 (44)		530 269(41)		530 287 (42)	
$\lvert R'_{hp}\rvert = \lvert\omega'_3/\omega'_p\rvert$	0.761 786 147 (29)				0.761 786 141 (28)			
Combined $\lvert R'_{hp}\rvert$	0.761786144(20)							
$\lvert\mu'_h\rvert$ (10^{-27} J T^{-1})	1.074553107(31)							

Sample magnetization dependence arises due to magnetic susceptibility and due to ^{3}He nuclear polarization. For perfectly spherical samples the average long-range contribution to the field anywhere in the sample vanishes [60]. Modeling the hyperpolarized ^{3}He gas in the stem as a magnetic dipole predicts ≈ 0.5 pT for 10% ^{3}He polarization, corresponding to a shift less than 15 μHz. The H_2O shape dependence is given by $\Delta\omega'_p/\omega'_p = \chi^{H_2O}(T)(1/3 - \epsilon)$ (SI units), where $\chi^{H_2O}(T)$ is the susceptibility. For an infinitely long cylinder perpendicular to $\vec{B}$, $\epsilon = 1/2$ and $\Delta\omega'_p = 93.10$ Hz; for a sphere, $\epsilon = 1/3$. Additional magnetization-dependent shifts have been revealed in recent studies with hyperpolarized ^{3}He-^{129}Xe mixtures used in a comagnetometer configuration [61–64]. Scaling these effects from Ref. [65] suggests shifts much less than 1 mHz.

Effects of the free-induction-decay signal (FID) frequency evolution due to dephasing in the nonuniform field are discussed by Refs. [66,67]. Studies with simulated FIDs using the measured magnetic field gradients indicate that these effects were less than 0.1 Hz and less than 0.01 Hz for the cylindrical and spherical H_2O probes and negligible for ^{3}He. Radiation damping shifts due to the current induced in the pickup coil were studied through the frequency dependence of ω_3^{uncor} over a set of five 23° pulses. Extrapolating the frequency dependence to zero longitudinal polarization sets an upper limit of 0.18 Hz on the shift. Radiation damping for the H_2O probes, studied by the longitudinal magnetization dependence over the five-pulse sequences and as the probe-tuning drifted, was negligible.

Temperature dependence of the H_2O diamagnetic shielding was corrected to 25 °C by measuring the temperature on the outside of the H_2O probe with a 1000 Ω platinum resistor (PT1000). Conservatively estimating an uncertainty of 5 Ω corresponding to 1°C resulted in 0.64 Hz uncertainty. From [68], $\chi^{H_2O}(T)$ was measured to change by 0.5% over 40°, which we interpret as $\partial\chi^{H_2O}/\partial T = 1.1 \times 10^{-9}$/°C, which adds an uncertainty of 0.02 Hz for the H_2O cylindrical probe.

Other corrections and uncertainties including higher-order time dependence and field fluctuations, for example moving equipment or tools, were estimated as the standard deviation of the residuals of the linear fits in Fig 3. Clock stability was found to be better than 0.01 Hz. The position reproducibility was 0.2 mm contributing an uncertainty 0.07 Hz for H_2O and 0.05 Hz for ^{3}He.

Conclusions—The final results of measurements of the corrected frequencies and corresponding absolute magnetic field determined by the ^{3}He and both H_2O probes are given in Table I. The absolute magnetic fields determined with ^{3}He and H_2O differ by 20 ± 41 ppb and 12 ± 41 ppb for

the spherical and cylindrical H_2O probes, respectively. Since the two H_2O probes with corrections consistent with those applied here [58] were used in the analysis of the E821 $g_\mu - 2$ measurements [48,49], this can be interpreted as confirming the calibration of the E821 magnetic-field measurement system to 16 ± 29 ppb, i.e., agreement better than 32 ppb (68% C.L.) compared to the 2.4 ppm tension of $a_\mu^{\rm exp}$ from E821 with the standard model $a_\mu^{\rm SM}$.

We can also use the corrected frequencies to determine $|R'_{hp}| = |\mu'_h/\mu'_p(25\,^\circ\mathrm{C})|$ and $|\mu'_h| = |R'_{hp}||\mu'_p(25^\circ)|$. The combined results for the two probes presented in Table I are consistent with Ref. [33] but with a 6.8 times larger uncertainty on $|R'_{hp}|$. (Both determinations of $|\mu'_h|$ use the shielded proton moment introducing a common uncertainty.) Straightforward improvements to the ^{3}He magnetometer materials, structure, and improved measurement of the corrections should lead to determination of $|R'_{hp}|$ at the few ppb level and provide a new method for absolute calibration of H_2O probes.

Most importantly, this work and improvements to our first-generation absolute ^{3}He magnetometer establish the technical basis for practical absolute magnetometry with ^{3}He and the establishment of a new magnetic field standard. Though this new standard would currently trace to measurements of μ'_h/μ'_p, the anticipated independent measurement of the helion moment [35] would provide a completely new magnetometry standard.

We are grateful to Sam Henry and Babak Abi for contributions during the initial stages of development. This work was supported by NSF Grant No. Phy-1812314, DOE Contract No. DE-AC02-06CH11357, and DOE Grant No. DE-FG02-88ER40415.

*Corresponding author.
chupp@umich.edu

[1] R. Körber *et al.*, Supercond. Sci. Technol. **29**, 113001 (2016).
[2] D. Budker and M. V. Romalis, Nat. Phys. **3**, 227 (2007).
[3] I. K. Kominis, T. W. Kornack, J. C. Allred, and M. V. Romalis, Nature (London) **422**, 596 (2003).
[4] P. Arpaia, G. Caiafa, and S. Russenschuck, Sci. Rep. **9**, 1491 (2019).
[5] Metrolab, https://www.metrolab.com.
[6] W. Phillips, W. Cooke, and D. Kleppner, Metrologia **13**, 179 (1977).
[7] P. J. Mohr, D. B. Newell, and B. N. Taylor, Rev. Mod. Phys. **88**, 035009 (2016); (2018 CODATA recommended values).
[8] H. Koch, G. Bison, Z. Grujić, W. Heil, M. Kasprzak, P. Knowles, A. Kraft, A. Pazgalev, A. Schnabel, J. Voigt, and A. Weis, Eur. Phys. J. D **69**, 262 (2015).
[9] See Supplemental Material at http://link.aps.org/supplemental/10.1103/PhysRevLett.124.223001 for providing technical and mathematical details of magnetometry standards, ^{3}He polarization, and NMR hardware and signal processing, which includes Refs. [10–32].
[10] D. Sundholm, J. Gauss, and A. Schäfer, J. Chem. Phys. **105**, 11051 (1996).
[11] S. G. Karshenboim and V. G. Ivanov, Phys. Lett. B **566**, 27 (2003).
[12] Y. I. Neronov and N. Seregin, Metrologia **51**, 54 (2014).
[13] B. Petley and R. Dondaldson, Metrologia **20**, 81 (1984).
[14] N. Nevo Dinur, O. J. Hernandez, S. Bacca, N. Barnea, C. Ji, S. Pastore, M. Piarulli, and R. B. Wiringa, Phys. Rev. C **99**, 034004 (2019).
[15] M. A. Bouchiat, T. R. Carver, and C. M. Varnum, Phys. Rev. Lett. **5**, 373 (1960).
[16] T. E. Chupp and K. P. Coulter, Phys. Rev. Lett. **55**, 1074 (1985).
[17] F. D. Colegrove, L. D. Schearer, and G. K. Walters, Phys. Rev. Lett. **8**, 439 (1962).
[18] T. R. Gentile, P. J. Nacher, B. Saam, and T. G. Walker, Rev. Mod. Phys. **89**, 045004 (2017).
[19] K. Coulter, T. E. Chupp, A. B. McDonald, C. D. Bowman, J. D. Bowman, J. J. Szymanski, V. Yuan, G. D. Cates, D. R. Benton, and E. D. Earle, Nucl. Instrum. Methods Phys. Res., Sect. A **288**, 463 (1990).
[20] E. Babcock, Z. Salhi, T. Theisselmann, D. Starostin, J. Schmeissner, A. Feoktystov, S. Mattauch, P. Pistel, A. Radulescu, and A. Ioffe, J. Phys. Conf. Ser. **711**, 012008 (2016).
[21] T. E. Chupp, R. A. Loveman, A. K. Thompson, A. M. Bernstein, and D. R. Tieger, Phys. Rev. C **45**, 915 (1992).
[22] A. Camsonne *et al.*, Phys. Rev. Lett. **119**, 162501 (2017).
[23] T. E. Chupp, P. Fierlinger, M. J. Ramsey-Musolf, and J. T. Singh, Rev. Mod. Phys. **91**, 015001 (2019).
[24] D. Bear, R. E. Stoner, R. L. Walsworth, V. A. Kostelecky, and C. D. Lane, Phys. Rev. Lett. **85**, 5038 (2000); **89**, 209902(E) (2002).
[25] R. Surkau *et al.*, Nucl. Instrum. Methods Phys. Res., Sect. A **384**, 444 (1997).
[26] F. Allmendinger, W. Heil, S. Karpuk, W. Kilian, A. Scharth, U. Schmidt, A. Schnabel, Yu. Sobolev, and K. Tullney, Phys. Rev. Lett. **112**, 110801 (2014).
[27] J. M. Wild *et al.*, Phys. Med. Biol. **47**, N185 (2002).
[28] J. Mulger and T. Altes, J. Magn. Reson. Imaging **37**, 313 (2013).
[29] G. D. Cates, S. R. Schaefer, and W. Happer, Phys. Rev. A **37**, 2877 (1988).
[30] D. D. McGregor, Phys. Rev. A **41**, 2631 (1990).
[31] T. E. Chupp, R. J. Hoare, R. L. Walsworth, and B. Wu, Phys. Rev. Lett. **72**, 2363 (1994).
[32] Y. Chibane, S. K. Lamoreaux, J. M. Pendlebury, and K. F. Smith, Meas. Sci. Technol. **6**, 1671 (1995).
[33] J. Flowers, B. Petley, and M. Richardson, Metrologia **30**, 75 (1993).
[34] Y. Neronov and N. Seregin, J. Exp. Theor. Phys. **115**, 777 (2012).
[35] A. Mooser, A. Rischka, A. Schneider, K. Blaum, S. Ulmer, and J. Walz, J. Phys. Conf. Ser. **1138**, 012004 (2018).
[36] A. Schneider, A. Mooser, A. Rischka, K. Blaum, S. Ulmer, and J. Walz, Ann. Phys. **531**, 1800485 (2019).
[37] G. Schneider *et al.*, Science **358**, 1081 (2017).
[38] C. Smorra *et al.*, Nature (London) **550**, 371 (2017).

[39] A. Rudzinski, M. Puchalski, and K. Pachucki, J. Chem. Phys. **130**, 244102 (2009).
[40] P. A. M. Dirac, Proc. R. Soc. A **117**, 610 (1928).
[41] J. Schwinger, Phys. Rev. **73**, 416 (1948).
[42] T. Aoyama, T. Kinoshita, and M. Nio, Phys. Rev. D **97**, 036001 (2018).
[43] T. Aoyama, M. Hayakawa, T. Kinoshita, and M. Nio, Phys. Rev. Lett. **109**, 111808 (2012).
[44] M. Davier, A. Hoecker, B. Malaescu, and Z. Zhang, Eur. Phys. J. C **80**, 241 (2020).
[45] A. Keshavarzi, D. Nomura, and T. Teubner, Phys. Rev. D **101**, 014029 (2020).
[46] J. Bailey *et al.* (CERN-Mainz-Daresbury Collaboration), Nucl. Phys. **B150**, 1 (1979).
[47] G. W. Bennett *et al.* (Muon g-2 Collaboration), Phys. Rev. D **73**, 072003 (2006).
[48] G. W. Bennett *et al.* (Muon g-2 Collaboration), Phys. Rev. Lett. **89**, 101804 (2002); **89**, 129903(E) (2002).
[49] G. W. Bennett *et al.* (Muon g-2 Collaboration), Phys. Rev. Lett. **92**, 161802 (2004).
[50] I. Logashenko *et al.* (Muon g-2 Collaboration), J. Phys. Chem. Ref. Data **44**, 031211 (2015).
[51] D. Hanneke, S. Fogwell, and G. Gabrielse, Phys. Rev. Lett. **100**, 120801 (2008).
[52] W. Liu, M. G. Boshier, S. Dhawan, O. vanDyck, P. Egan, X. Fei *et al.*, Phys. Rev. Lett. **82**, 711 (1999).
[53] M. Abboud, A. Sinatra, X. Maître, G. Tastevin, and P.-J. Nacher, Europhys. Lett. **68**, 480 (2004).
[54] A. Nikiel, P. Blümler, W. Heil, M. Hehn, S. Karpuk, A. Maul, E. Otten, L. Schreiber, and M. Terekhov, Eur. Phys. J. D **68**, 330 (2014).
[55] W. Heil, in *High Sensitivity Magnetometers*, edited by A. Grosz, M. Haji-Sheikh, and S. Mukhopadhyay (Springer, Cham, Switzerland, 2017), Vol. 19, pp. 493–521.
[56] Keopsys.com Model CYFL-GIGA.
[57] J. Maxwell, C. Epstein, and R. Milner, Nucl. Instrum. Methods Phys. Res., Sect. A **764**, 215 (2014).
[58] X. Fei, V. W. Hughes, and R. Prigl, Nucl. Instrum. Methods Phys. Res., Sect. A **394**, 349 (1997).
[59] M. Fertl, Fermilab E989 internal, 2014.
[60] J. H. Wesenberg and K. Mølmer, Phys. Rev. Lett. **93**, 143903 (2004).
[61] M. V. Romalis, D. Sheng, B. Saam, and T. G. Walker, Phys. Rev. Lett. **113**, 188901 (2014).
[62] D. Sheng, A. Kabcenell, and M. V. Romalis, Phys. Rev. Lett. **113**, 163002 (2014).
[63] M. E. Limes, N. Dural, M. V. Romalis, E. L. Foley, T. W. Kornack, A. Nelson, L. R. Grisham, and J. Vaara, Phys. Rev. A **100**, 010501(R) (2019).
[64] W. A. Terrano, J. Meinel, N. Sachdeva, T. E. Chupp, S. Degenkolb, P. Fierlinger, F. Kuchler, and J. T. Singh, Phys. Rev. A **100**, 012502 (2019).
[65] N. Sachdeva, I. Fan, E. Babcock, M. Burghoff, T. E. Chupp, S. Degenkolb *et al.*, Phys. Rev. Lett. **123**, 143003 (2019).
[66] J. Flowers, P. Franks, and B. Petley, IEEE Trans. Instrum. Meas. **44**, 488 (1995).
[67] B. Cowan, Meas. Sci. Technol. **7**, 690 (1996).
[68] J. S. Philo and W. M. Fairbank, J. Chem. Phys. **72**, 4429 (1980).

Supplemental Material for: Absolute magnetometry with ^{3}He

Midhat Farooq,[1] Timothy Chupp,[1] Joe Grange,[1,2] Alec Tewsley-Booth,[1]
David Flay,[3] David Kawall,[3] Natasha Sachdeva,[1] and Peter Winter[2]

[1] *Physics Department, University of Michigan, Ann Arbor, MI 48109 USA*
[2] *Argonne National Laboratory, Lemont, IL 60439 USA*
[3] *Physics Department, University of Massachusetts, Amherst, MA 01003 USA*

(Dated: October 25, 2021)

MAGNETOMETRY STANDARDS

Quantities used to determine the shielded proton and shielded helion magnetic moments are provided in (see Table I).

H_2O

The shielded magnetic moment of protons in H_2O μ'_p was determined from the ratio of the proton NMR frequency to the hydrogen-maser frequency at 34.7°C in the same magnetic field providing the ratio [1]

$$\frac{\mu'_p(34.7^\circ\mathrm{C})}{\mu_e(H)} = -1.519258095(16)\times10^{-3}. \tag{.1}$$

The temperature dependence of μ'_p was separately measured over the range 5°C to 45°C and found to vary linearly as [2],

$$\frac{1}{\mu'_p}\frac{d\mu'_p}{dT} = -10.36(30)\times10^{-9}. \tag{.2}$$

The ratio of the free and bound-state g-factors of the electron in the H-atom has been precisely calculated [3] and evaluated [4] (see Table I).

$$\frac{\mu_e(H)}{\mu_e} = \frac{g_e(H)}{g_e} = 1 - 17.7054\times10^{-6}. \tag{.3}$$

These can be combined to provide,

$$\frac{\mu'_p(25^\circ\mathrm{C})}{\mu_e} = -1.519\ 231\ 348(17)\times10^{-3}\ (10.9\ \mathrm{ppb}). \tag{.4}$$

The electron magnetic moment is

$$\mu_e = \frac{g_e}{2}\mu_B = -9.284\ 764\ 704\ 3(28)\times10^{-24}\mathrm{JT}^{-1}\ (0.3\ \mathrm{ppb}), \tag{.5}$$

where $\mu_B = \frac{e}{m_e}\frac{\hbar}{2}$ is the Bohr magneton. The relative uncertainty of μ_B and thus μ_e is mostly due to uncertainties in e and m_e ($\hbar$ is fixed in SI units [4]), since the relative uncertainty on g_e is 0.28 ppt [5]. Thus for a spherical H_2O sample at the standard reference temperature of 25°C

$$\mu'_p(25^\circ) = 1.410\ 570\ 560(15)\times10^{-26}\ \mathrm{JT}^{-1}\ (10.9\ \mathrm{ppb}). \tag{.6}$$

This is consistent with the 2018 CODATA evaluation [4].

Recently the difference of diamagnetic shielding for protons in H_2 and H_2O was measured with the result $\Delta_\sigma = \sigma^{H_2} - \sigma^{H_2O} = 680.0(1.5)\times10^{-9}$ at 25°C [6]. Combined with a calculated diamagnetic shielding correction $\sigma^{H_2} = 26.288(2)\times10^{-6}$ [8] yields $\sigma_p^{H_2O}(25^\circ\ \mathrm{C}) = 25.680(2)\times10^{-6}$ resulting in $\mu'_p = 1.410\ 570\ 575\ 7(53)\times10^{-26}\ \mathrm{JT}^{-1}$ (3.8 ppb), which

is more precise but shifts μ'_p by 11 ppb. An alternative determination of μ'_p would use the recent direct 0.3 ppb measurement of the proton magnetic moment g factor [7] using $\sigma_p^{\mathrm{H_2O}}(25^\circ\ \mathrm{C})$ adopted by CODATA [4],

$$\begin{aligned}\mu'_p &= g_p \mu_N [1 - \sigma^{\mathrm{H_2O}}(25^\circ\mathrm{C})] \\ &= 1.410\ 570\ 555\ 7(155) \times 10^{-26}\mathrm{JT}^{-1}\ (11.0\ \mathrm{ppb}).\end{aligned} \tag{.7}$$

A third route to μ'_p is provided by direct measurement of the ^{3}He nucleus magnetic moment μ_h combined with the calculated diamagnetic-shielding and measurement of μ'_h/μ'_p as provided by [9] and extensions of this work.

^{3}He

For ^{3}He, the shielded atomic magnetic moment μ'_h has been most precisely measured in terms of the shielded proton magnetic moment in water [9] (4.3 ppb) and protons in high-pressure H_2 [10] (2.6 ppb).

$$\frac{\mu'_h}{\mu'_p(25^\circ\mathrm{C})} = -0.761\ 786\ 1313(33)\ (4.3\ \mathrm{ppb}) \tag{.8}$$

$$\frac{\mu'_h}{\mu_p^{\mathrm{H_2}}} = -0.761\ 786\ 594\ (2) \quad (2.6\ \mathrm{ppb}) \tag{.9}$$

While CODATA [4] uses only Ref. [9], these results are consistent when taking into account ratios of shielded-proton in H_2O [1, 2] and in H_2 [8] to the electron magnetic moments

$$\frac{\mu'_h}{\mu_p^{\mathrm{H_2}}} \times \frac{1 - \sigma_p^{\mathrm{H_2}}}{1 - \sigma_p^{\mathrm{H_2O}}(25^\circ\mathrm{C})} = -0.761\ 786\ 139\ 2(83). \tag{.10}$$

Combining eq. .8 with eq .4 and μ_e (eq .5):

$$\mu'_h = \left(\frac{\mu'_h}{\mu'_p(25^\circ\mathrm{C})}\right)\left(\frac{\mu'_p(25^\circ\mathrm{C})}{\mu_e}\right)\mu_e = -1.074553090(13) \times 10^{-26}\ \mathrm{JT}^{-1}\ (11.4\ \mathrm{ppb}). \tag{.11}$$

The uncertainty is dominated by the uncertainty on μ'_p/μ_e [1, 4], which is also the dominant source of uncertainty in $\sigma_p^{\mathrm{H_2O}}$ in eq. .10.

Direct measurement of the helion magnetic moment μ_h would eliminate the proton from the chain. Work is underway [11, 12] to directly measure μ_h and the the bound-state magnetic moment of hydrogen-like ^{3}He$^+$ in a Penning trap with techniques similar to those used to measure the proton [7] and antiproton [13] g-factors. The high-precision theoretical calculation of the diamagnetic shielding of μ_h in the neutral atom [14], would provide the shielded magnetic moment μ'_h at the few ppb level. The bound-state magnetic moment of hydrogen-like ^{3}He$^+$ is about 1000-times larger than the nuclear moment, and can be correspondingly more precisely measured, however extracting μ'_h requires bound-state quantum electrodynamics (QED) correctionsand accounting of the short-range magnetization within the nucleus, the Zemach moment [15]. One or both of these approaches would provide independent determination of μ'_h at the few ppb level.

^{3}HE POLARIZATION

Magnetometer signals depend on the sample magnetization, $|M_N| = |\mu_N|[N]P_N$, for a nuclear species with magnetic moment μ_N, concentration $[N]$, and the polarization P_N, the fractional difference of spin-up and spin-down concentrations. For protons in a sample at temperature T, the polarization is proportional to the magnetic field strength and for $P_p \ll 1$ is given by $P_p \approx \mu_p B/kT$, where k is Boltzmann's constant. At $T = 300K$ and $B = 1$ T, $P_p \approx 4 \times 10^{-6}$. For ^{3}He polarized by optical pumping, the polarization is *independent* of the magnetic field and P_3 can be 10^5 or even more times larger than P_p providing comparable magnetization and magnetometry signals at 1 T.

Two optical pumping techniques are used for hyperpolarization of ^{3}He: spin-exchange with optically pumped alkali or SEOP [16, 17] and metastability exchange or MEOP [18]. Both can produce polarizations as large as 70-80% [19].

Quantity	value	ppb	Ref.
$\frac{\mu_p'(34.7^\circ\mathrm{C})}{\mu_e(H)}$ (10^{-3})	$-1.519258095(16)$	10.5	[1]
$\frac{1}{\mu_p'}\frac{d\mu_p'}{dT}$ (10^{-9})	$-10.36(30)$	0.3	[2]
$\frac{\mu_e(H)}{\mu_e}$	$1 - 17.7054 \times 10^{-6}$		[3]
μ_e (JT^{-1})	$-9.284\ 764\ 704\ 3(28) \times 10^{-24}$	0.3	[4]
$\mu_p'(25^\circ\mathrm{C})$ (JT^{-1})	$1.410\ 570\ 560\ \ (15) \times 10^{-26}$	11.3	
$\frac{\mu_h'}{\mu_p'(25^\circ\mathrm{C})}$	$-0.761\ 786\ 1313\,(33)$	4.3	[9]
$\frac{\mu_h'}{\mu_e}(10^{-3})$	$1.157\ 329\ 372\ \ (13)$	11.3	
μ_h' (JT^{-1})	$-1.074\ 553\ 090\ \ (12) \times 10^{-26}$	11.4	

TABLE I. Quantities used to determine μ_h' and $\mu_p'(25^\circ)$.

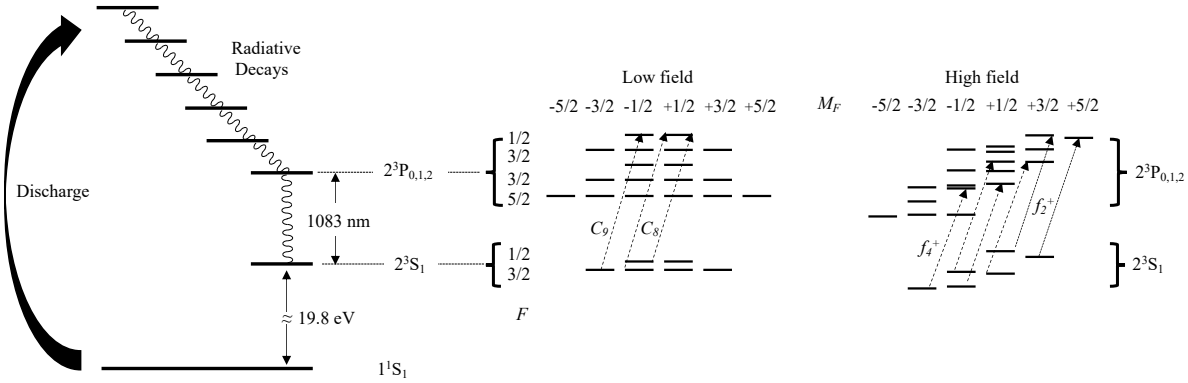

FIG. 1. Energy levels relevant to excitation and optical pumping of metastable ^{3}He (left). Transitions near 1083 nm that produce nuclear polarization for low and high magnetic field for σ_+ light are shown; the vertical scales are relative and different for low field and high field. See Ref. [32] for more details.

SEOP has been most useful for producing large samples of highly polarized ^{3}He for neutron polarization [20, 21] and polarized targets used in electron scattering [22, 23] and also for polarizing separately or simultaneously other noble gases, notably ^{129}Xe [24] for studies of fundamental forces that would produce an permanent electric dipole moment [25] or exotic couplings to nuclear spin [26]. MEOP polarization of ^{3}He has also been used in neutron polarization and polarimetry [27] and fundamental physics studies [28, 29]. Magnetic resonance imaging using hyperpolarized gas has used both techniques for ^{3}He [30] and SEOP for ^{129}Xe [31].

In spite of overlapping applications, several characteristics distinguish the techniques. SEOP is practical for polarizing concentrations corresponding to pressures across a broad range up to many atmospheres, but requires a mixture of gases, typically including N_2 along with the alkali-metal, which is usually Rb or a mixture of alkali metals and requires many hours to build up ^{3}He polarization. MEOP polarizes samples of pure helium or pure ^{3}He at relatively low pressures of a few to tens of torr with characteristic times of minutes or less. MEOP is the best approach for development of practical absolute magnetometers because pure ^{3}He minimizes magnetic perturbations and the polarization times allow high repetition rate for measurements.

MEOP has been extensively studied, most recently at high magnetic fields (1.5 T) relevant to this work [32–34]. The relevant levels of ^{3}He for MEOP are shown in Fig. 1. The ≈ 19.8 eV energy splitting from the ground state to higher states is not practically accessible with photons, and a discharge produces excited states, which decay to populate the metastable $J = 1$ electron-spin triplet $^3S_1$ state. For ^{3}He, which has nuclear spin $I = 1/2$, the total angular momentum in the metastable state is $F = J \pm 1/2$. The levels are labeled by F for low magnetic field and by the magnetic quantum number m_F for high magnetic field. In either case, circularly polarized laser light induces $\Delta m_F = +1$ transitions (for σ_+ light), thus *pumping* the population of metastable atoms out of the lower m_F states. This population of metastable atoms has nuclear polarization, which is transferred to ground-state atoms in collisions which exchange the metastable excitation and preserve nuclear polarization.

CELL PRODUCTION

The ^{3}He cells were blown borosilicate (PYREX) glass, approximately spherical with 2.5 cm diameter. Tubes connected the glass spheres to a manifold that connected them to a vacuum and gas-handling system. The cells were cleaned with soap and/or a solution of H_2SO_4 and H_2O_2 (Piranha) before connecting to the vacuum system. Once evacuated, the cells were baked at 200° for several days before filling with ^{3}He. The ^{3}He was nominally 99.99% helium with 99% ^{3}He enrichment and was purified by flowing through a heated alkali getter [35]. With a few torr of gas in a cell, a discharge was struck to further clean the cells and to analyze the gas purity by monitoring the discharge with a fiber-optic coupled spectrometer [36]. Generally, clean gas was introduced into the cells after several cycles of discharge cleaning. Further purification of the gas was provided by cooling a separate portion of the gas-filled manifold, with liquid N_2 for 20-30 minutes. With the desired pressure in the manifold the cell was pulled off by sealing with a torch leaving a stem several mm long that broke the nominal spherical symmetry. The estimated effect of the non-spherical sample and container and the stem are discussed below.

NMR CONTROLLER AND DAQ

The NMR controller and data acquisition are shown in Fig. 2. The probe NMR coils provided both the pulse to tip the magnetization and inductive pick-up and were tuned and impedance matched to 50Ω with parallel and series non-magnetic capacitors. A single coaxial cable was connected to a high-powered single-pole-double-throw (SPDT) switch normally connected to a blanking switch, bandpass filter for 48 MHz (BPF), 24 dB preamplifier, and mixer. The NMR pulse signal and the 1 V amplitude mixer reference signal were provided by the same frequency synthesizer, which was set to ω_h^{ref}, below the ^{3}He free precession frequency. The mixed-down frequency, usually 100-300 Hz, was lowpass filtered, further amplified by 40 dB and digitized at 10 kHz with a 16-bit ADC. The NMR pulse that tipped the ^{3}He magnetization was provided by a 50 dB pulse amplifier [37] with pulse durations of 1-4 μs, and the tip angle was varied by changing the pulse durations or the RF amplitude. The NMR tip angles were ≈23° for ^{3}He and ≈90° for H_2O probes. The smaller tip angle for ^{3}He leaves about 90% of the original longitudinal polarization after each pulse providing comparable signal sizes for a series of FIDs but also a variation of the longitudinal and transverse polarization for systematic studies. The 90° or $\pi/2$ pulse for protons maximized the signal size.

NMR SIGNAL PROCESSING

Raw data from a typical free-induction (FID) decay signals are shown in Fig. 3. The mixed-down FID frequencies as a function of time t were estimated with a non-linear least-squares fit to $S(t) = A0 + A_1 \cos(\omega t + \phi_0) \exp(-t/T_2^*)$, where A_0 corresponds to the electronics' offset, A_1 is the FID amplitude, ω is the FID frequency, ϕ_0 is the FID phase offset at the nominal $t = 0$, and T_2^* represents free-precession relaxation time. The FID model is justified for ^{3}He because dephasing of spins moving in the non-uniform magnetic field was dominated by diffusion [38, 39]. Based on the measured noise in the absence of signals, the χ^2 and the uncertainty on ω were consistent with expectations [40, 41]. The proton channel FID, is not accurately represented by an exponentially decaying sinusoid because in H_2O the molecules do not diffuse significantly in the magnetic-field gradient during the course of the FID. Thus the raw time-domain data were multiplied by an exponential damping function as shown. Studies of the effect of varying the damping time showed negligible change of the best fit frequency. For the cross calibration, a blind analysis was effected by adding a frequency generated from a hidden random number to one of the fit frequencies (proton/^{3}He channels, respectively for the spherical/cylindrical probes). Once all systematic studies were completed and the corrections and uncertainties finalized for each study, the blind was removed providing the final frequencies.

[1] W. Phillips, W. Cooke, and D. Kleppner, Metrologia **13**, 179 (1977).
[2] B. Petley and R. Dondaldson, Metrologia **20**, 21 (1984).
[3] S. G. Karshenboim and V. G. Ivanov, Phys. Lett. **B566**, 27 (2003).
[4] P. J. Mohr, D. B. Newell, and B. N. Taylor, Rev. Mod. Phys. **88**, 035009 (2016), (2018 CODATA recommended values).
[5] D. Hanneke, S. Fogwell and G. Gabrielse, Phys. Rev. Lett. **100**, 120801 (2008).
[6] Y. I. Neronov and N. Seregin, Metrologia **51**, 54 (2014).
[7] G. Schneider *et al.*, Science **358**, 1081 (2017).

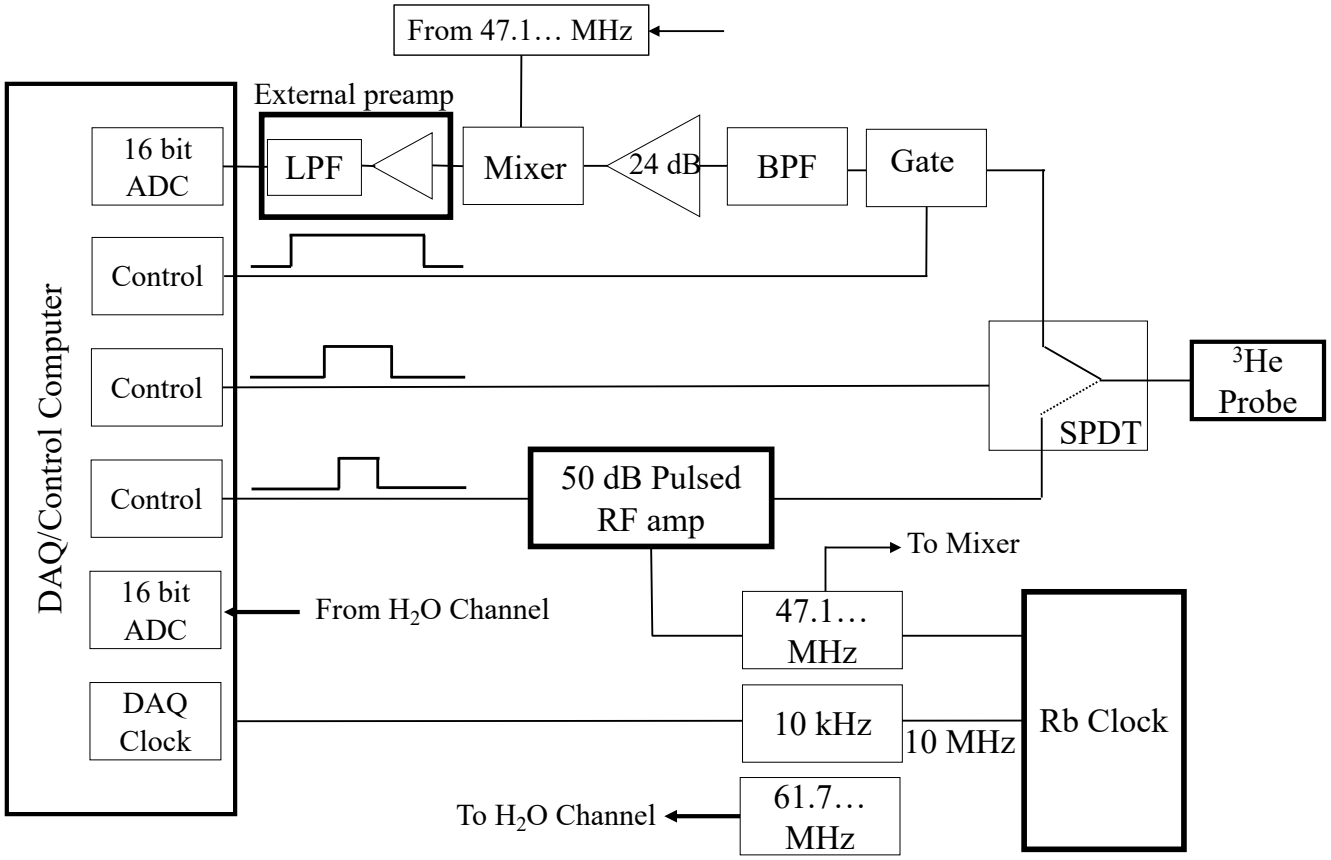

FIG. 2. Schematic of the NMR Controller and data acquisition setup described in the text.

[8] D. Sundholm, J. Gauss, and A. Schäfer, The Journal of Chemical Physics **105**, 11051 (1996).
[9] J. Flowers, B. Petley, and M. Richardson, Metrologia **30**, 7 (1993).
[10] Y. Neronov and N. Seregin, J. of Exp. and Theo. Phys. **115**, 115 (2012).
[11] A. Mooser, A. Rischka, A. Schneider, K. Blaum, S. Ulmer, and J. Walz, Journal of Physics: Conference Series **1138**, 012004 (2018).
[12] A. Schneider, A. Mooser, A. Rischka, K. Blaum, S. Ulmer, and J. Walz, Annalen der Physik , 1800485 (2019).
[13] C. Smorra *et al.*, Nature **550**, 371 (2017).
[14] A. Rudzinski, M. Puchalski, and K. Pachucki, Journal of Chemical Physics **130**, 244102 (2009).
[15] N. Nevo Dinur, O. J. Hernandez, S. Bacca, N. Barnea, C. Ji, S. Pastore, M. Piarulli, and R. B. Wiringa, Phys. Rev. C **99**, 034004 (2019).
[16] M. A. Bouchiat, T. R. Carver, and C. M. Varnum, Phys. Rev. Lett. **5**, 373 (1960).
[17] T. E. Chupp and K. P. Coulter, Phys. Rev. Lett. **55**, 1074 (1985).
[18] F. D. Colegrove, L. D. Schearer, and G. K. Walters, Phys. Rev. Lett. **8**, 439 (1962).
[19] T. R. Gentile, P. J. Nacher, B. Saam, and T. G. Walker, Rev. Mod. Phys. **89**, 045004 (2017).
[20] K. Coulter *et al.*, Nucl. Inst. and Meth. in Phys. Res. A **288**, 463 (1990).
[21] E. Babcock *et al.*, Journal of Physics: Conference Series **711**, 012008 (2016).
[22] T. E. Chupp, R. A. Loveman, A. K. Thompson, A. M. Bernstein, and D. R. Tieger, Phys. Rev. **C45**, 915 (1992).
[23] A. Camsonne *et al.*, Phys. Rev. Lett. **119**, 162501 (2017).
[24] N. Sachdeva, I. Fan, E. Babcock, M. Burghoff, T. E. Chupp, S. Degenkolb, *et al.*, Phys. Rev. Lett. **123**, 143003 (2019).
[25] T. E. Chupp, P. Fierlinger, M. J. Ramsey-Musolf, and J. T. Singh, Rev. Mod. Phys. **91**, 015001 (2019).
[26] D. Bear, R. E. Stoner, R. L. Walsworth, V. A. Kostelecky, and C. D. Lane, Phys. Rev. Lett. **85**, 5038 (2000), [Erratum: Phys. Rev. Lett. 89, 209902(E) (2002)].
[27] R. Surkau *et al.*, Nuc. Inst. and Meth. **A384**, 444 (1997).
[28] F. Allmendinger, W. Heil, S. Karpuk, W. Kilian, A. Scharth, U. Schmidt, A. Schnabel, Yu. Sobolev, and K. Tullney, Phys. Rev. Lett. **112**, 110801 (2014).
[29] M. V. Romalis, D. Sheng, B. Saam, and T. G. Walker, Phys. Rev. Lett. **113**, 188901 (2014).
[30] J. M. Wild *et al.*, Physics in Medicine and Biology **47**, N185 (2002).
[31] J. Mulger and T. Altes, J. Magn. Reson. Imaging **37**, 313 (2013).
[32] M. Abboud, A. Sinatra, X. .Maître, G. Tastevin, and P.-J. Nacher, Europhysics Letters (EPL) **68**, 480 (2004).

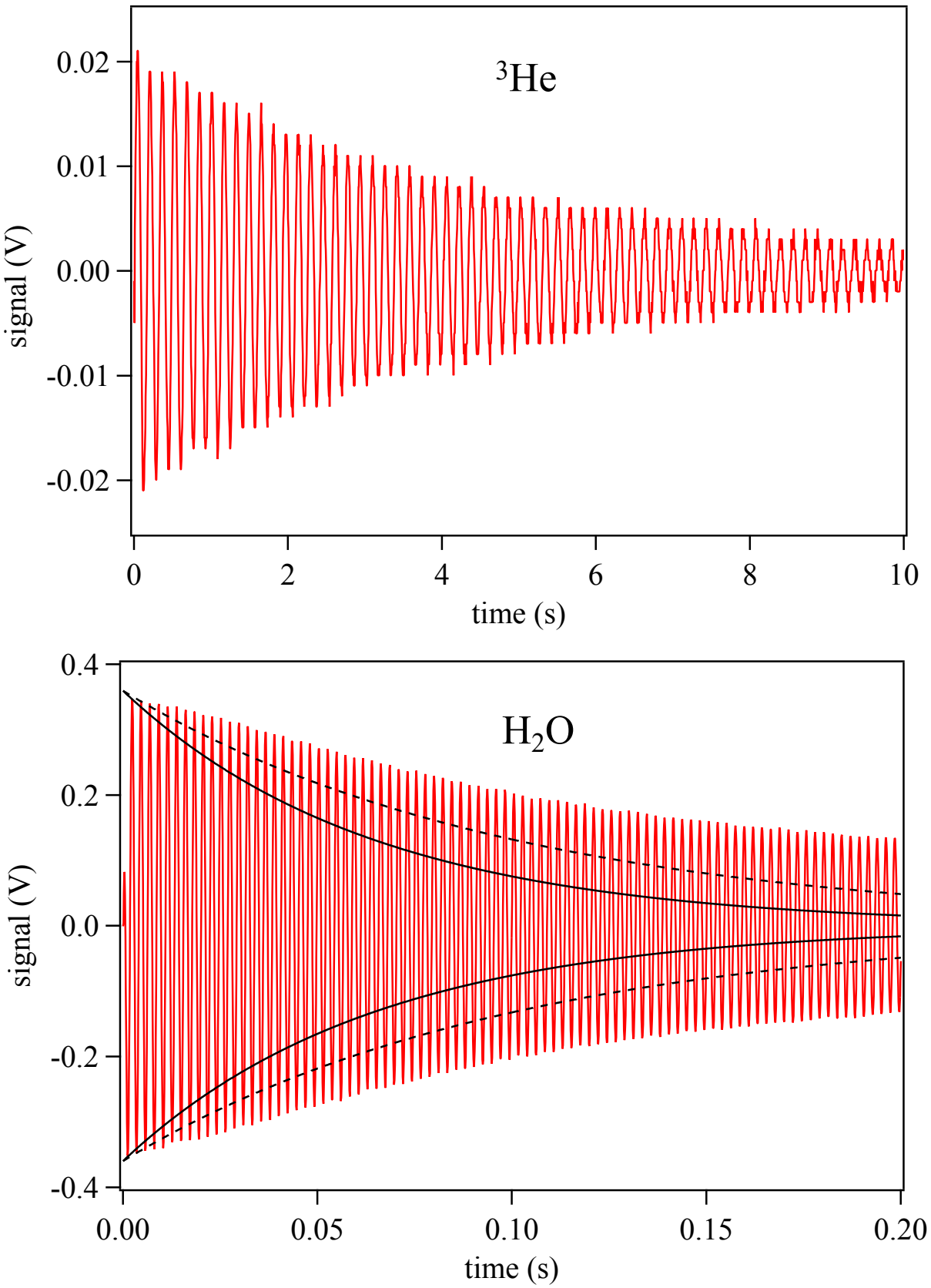

FIG. 3. FIDs for ^{3}He and the spherical H_2O sample. Offsets have been removed. The non-exponential time dependence of the H_2O discussed in the text is evident; the damping function is shown as a dashed black line and the resulting used to fit the FID is shown as a solid black line.

[33] A. Nikiel, P. Blümler, W. Heil, M. Hehn, S. Karpuk, A. Maul, E. Otten, L. Schreiber, and M. Terekhov, Eur. Phys. J. **D68**, 330 (2014).
[34] W. Heil, in *High Sensitivity Magnetometers*, Vol. 19, edited by A. Grosz, M. Haji-Sheikh, and S. Mukhopadhyay (Springer, Cham, Switzerland, 2017) pp. 493–521.
[35] SAES.com.
[36] OceanOptics.com.
[37] TOMCO.com Model BT00250Gamma.
[38] G. D. Cates, S. R. Schaefer, and W. Happer, Phys. Rev. **A37**, 2877 (1988).
[39] D. D. McGregor, Phys. Rev. A **41**, 2631 (1990).
[40] T. E. Chupp, R. J. Hoare, R. L. Walsworth, and B. Wu, Phys. Rev. Lett. **72**, 2363 (1994).
[41] Y. Chibane, S. K. Lamoreaux, J. M. Pendlebury, and K. F. Smith, Measurement Science and Technology **6**, 1671 (1995).